Mechanical Systems and Signal Processing 224 (2025) 112080

Contents lists available at ScienceDirect

Mechanical Systems and Signal Processing

journal homepage: www.elsevier.com/locate/ymssp

Directional DIC method with automatic feature selection

Thijs Masmeijer [a], Ed Habtour [a,*], Klemen Zaletelj [b], Janko Slavič [b]

[a] University of Washington, William E. Boeing Department of Aeronautics and Astronautics, 3940 Benton Lane NE Guggenheim Hall, Seattle, WA, 98195, United States of America

[b] University of Ljubljana, Faculty of Mechanical Engineering, Aškerčeva cesta 6, 1000, Ljubljana, Slovenia

ARTICLE INFO

Communicated by M. Brake

Keywords:
Image-based structural identification
DIC
Directional DIC
Optical flow

ABSTRACT

Using displacement identification via high-speed cameras is a non-contact, full-field technique for characterizing the dynamic properties of engineered structures. Achieving reliable measurements of structural deformation through conventional Digital Image Correlation (DIC) requires a well-defined spatial gradient in two orthogonal directions within an image subset of pixels. However, DIC is susceptible to the aperture problem, which leads to an ill-conditioned optimization problem. An example of such a case is cable systems on which no speckle patterns can be applied. This study proposes Directional DIC (D-DIC) as an alternative technique to overcome the limitations posed by the aperture problem in conventional DIC methods. Directional DIC assumes the local direction of motion, which is often a valid assumption in structural vibration tests, as individual vibration shapes are often unidirectional at localized parts of the structure. This alleviates some restrictions on trackable image subsets, enabling more trackable locations. A parameter for quantifying expected tracking performance for D-DIC is introduced. The parameter enables automatic feature selection for D-DIC, making optical methods more accessible for displacement identification on structures where no speckle patterns can be applied. Experimental modal tests are conducted using a flexible spider web-like structure to validate the D-DIC method and compare it to conventional DIC. The experimental findings show that the Directional DIC method allows for measuring displacements at significantly more locations than conventional DIC. Additionally, D-DIC provided less noisy frequency response functions, more retrieved stable poles, and more fitted vibrational modes. Lastly, the findings show that D-DIC is especially superior to DIC when using small subsets since D-DIC is less inhibited by the aperture problem.

1. Introduction

Measuring vibrations of engineering structures and mechanical systems is fundamental to conducting structural diagnostics, prognostics, reliability analysis, and service-life management [1–3]. However, installing physical sensors can be costly, complex, or intrusive for large or highly deformable structures. Non-contact displacement measurements based on computer vision offer significant advantages over contact sensors, which include full-field displacement and eliminating the added mass of physical sensors that often alter the dynamic characteristics of the structure [4,5]. Non-contact displacement measurements are advantageous for testing and evaluating flexible structures, such as aircraft wings, wind turbines, suspension bridges, cables, and soft robots. Several image alignment techniques have been introduced to provide not only the dynamic responses of a structure but also the deformation or modal shapes from extracted video motions. One of the most widely used image alignment techniques is the Lucas–Kanade

* Corresponding author.
E-mail address: habtour@uw.edu (E. Habtour).

https://doi.org/10.1016/j.ymssp.2024.112080
Received 17 July 2024; Received in revised form 8 October 2024; Accepted 19 October 2024
Available online 21 November 2024

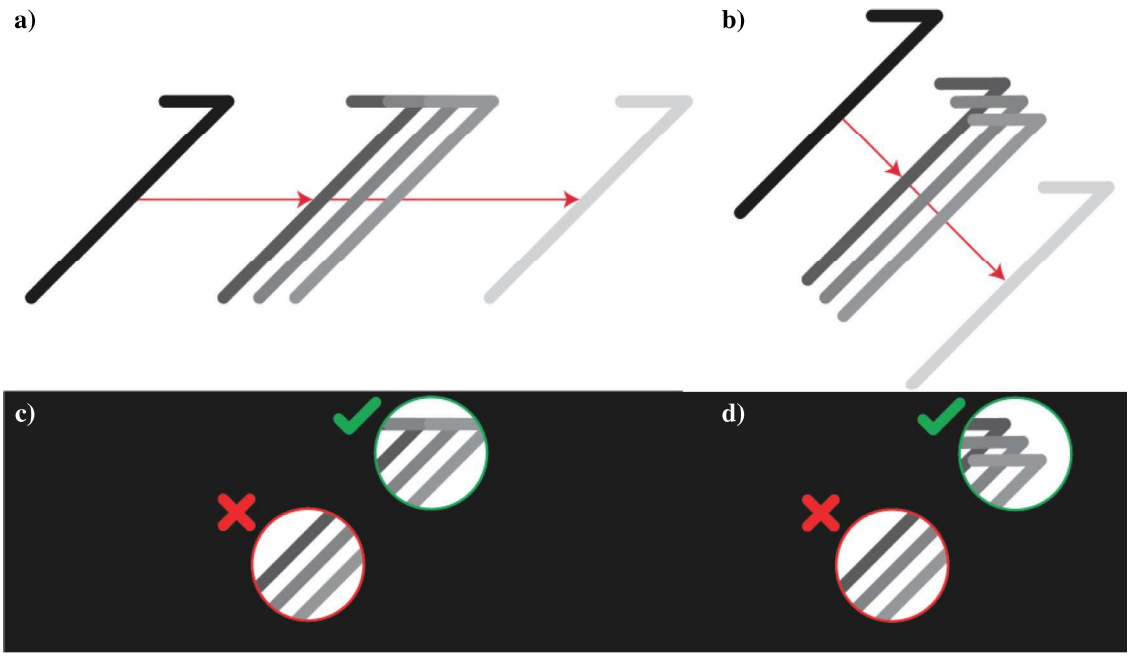

Fig. 1. The aperture problem. An object moves horizontally (a) and diagonally (b). When observing an edge through a small hole (an aperture), the horizontal motion (c) and the diagonal motion (d) are indistinguishable. However, when the aperture observes a corner, unique motions are detected, thus overcoming the aperture problem.

optical flow algorithm [6,7]. Peters et al. [8] introduced the method into engineering as Digital Image Correlation (DIC). DIC has been widely used in experimental mechanics since it was first applied in the field of structural dynamics in 1983 [9,10]. Current implementations of the Lucas–Kanade method in DIC have improved accuracy by including root-finding techniques to minimize residuals and can warp images for better alignment [7,11]. Alternatives to DIC consisted of methods such as photogrammetry point tracking [12–15], phase-based methods [16–18], and the complex pyramid method [19]. Since vibration shapes are often required in 3D space Siebert et al. [20] demonstrated the retrieval of 3D full-field displacement responses of a structure using DIC with multiple time-synchronized cameras. Gorjup et al. [21] used triangulation in the frequency domain to obtain 3D vibration mode shapes using a single camera. An FEM model was used as an alternative to synchronized cameras for finding the 3D vibration shapes [22]. The utility of DIC to extract 3D mode shapes is now commonplace in structural vibration [21–27] since computer vision-based can provide mode-shape magnification in structural vibration [28–30], FEM model updating [31–33], damage precursors identification [15,34–36], and estimating moving forces for structural health monitoring [37]. High-speed infrared cameras were employed to identify the full field strain mode shapes of beams using the thermoelastic relationship and using individual pixels as sensors [38]. By using an inertial measurement unit (IMU), any 6-DOF motion was corrected for motion estimation with optical methods [39]. Readers interested in further information about the application of optical DIC methods in the field of structural vibrations are encouraged to refer to excellent review publications by Niezrecki et al. [40], and Baqersad et al. [41].

Obtaining reliable displacement measurements with DIC requires an image subset (feature) to have a well-defined gradient in two orthogonal directions. However, most engineering structures lack surfaces with such well-defined gradients. The lack of sufficient gradient in one of the directions in a subset makes it challenging to observe the motion in that direction correctly. Fig. 1 provides a visual explanation of this well-known phenomenon called the aperture problem, which causes an ill-conditioned optimization problem in DIC [42–44]. To overcome the aperture problem, it is common to apply speckle patterns to the test samples to track the material displacement [45].

There are several reasons why speckle patterns in the form of permanent paint or temporary stickers may not always be suitable for a structure. For example, measuring the displacement of a cable, or a network of cables presents a challenge, as no speckle pattern can be applied [46]. In such cases, there will only be a large gradient perpendicular to the cable, between the cable and the background. Other reasons range from undesirable aesthetics and cost of the speckle application to a civil structure [19] and its influence on the aerodynamic properties of an aerospace structure [47]. Nonetheless, the main advantage of non-contact methods, such as optical methods, is that the mass of the sensor will not alter the vibration characteristics of the structure [48]. For the same reasons, applying paint or stickers to very lightweight and flexible structures is undesirable. These examples highlight the need for a displacement tracking method with less restrictive requirements for trackable image subsets. Quantifying the expected tracking performance of these subsets is crucial for enabling the identification of naturally occurring features. Automatic feature detection algorithms can be utilized to localize pixel subsets in an image that can adequately track the displacement. One of the earliest automatic feature detection algorithms was based on the image gradients in four directions [49]. Tomasi et al. [50,51]

introduced an influential approach that computed the eigenvalues of a pixel subset to score its expected performance, taking both sensitivity and stability into account. Feature detection algorithms continued to evolve and offered faster computations and enhanced robustness against edge-like features [52,53], or reduced the effects of 1D edges [54]. Generally, selection algorithms choose features in descending order of score and minimum distance between them [50,51], select features where scores have local maxima [49,52], or use Adaptive Non-Maximal Suppression (ANMS) to ensure features are more evenly distributed across an image [53].

Javh et al. [55] introduced the Simplified Optical Flow method (SOF) as an alternative to the Lucas–Kanade optical flow algorithm to measure displacement for structural vibration. The SOF method overcame the aperture problem by taking advantage of the fact that the pixel intensity gradient is constant and uni-directional for low (sub-pixel) amplitudes. Patterns on measured structures were designed such that the motion was in the direction of the pixel intensity gradient, enabling individual pixels (or small subsets of pixels) to be utilized as one-degree-of-motion displacement sensors. The method significantly sped up the measurements and demonstrated a high displacement resolution of 0.0008 pixels. However, SOF is limited to low (sub-pixel) amplitudes, thus restricting its effectiveness. Additionally, SOF does not include a root-finding algorithm to refine the extracted motion, unlike Lucas–Kanade, which incorporates a root-finding capability for this purpose [56,57].

To overcome the limitations of the DIC and SOF methods stated above, this study proposes the Directional DIC (D-DIC) as an alternative method that retrieves motion via a user-defined direction. The proposed D-DIC method can leverage root-finding methods, ensuring accurate high-displacement measurements. A *priori* motion direction produces fewer restrictions on selecting tracking locations by minimizing the aperture problem. As the new method has different restrictions on trackable regions, a new parameter, λ_{d}, is introduced to quantify expected tracking performance, thus enabling automatic feature selection for D-DIC. The D-DIC method is publicly available through the OpenSource Python package pyIDI [58]

This article is organized as follows. First, a theoretical background is given on DIC and automatic feature selection in Section 2. The D-DIC method and parameter λ_{d} are detailed in Section 3. The experimental approach and validation of the D-DIC method are provided in Section 4. The section also provides a detailed comparison between the Directional and conventional DIC methods. The major findings of this study are summarized in the conclusion section.

2. Theoretical background

This section details the mathematical implementation of DIC for measuring displacements from a sequence of images and corresponding automatic feature selection algorithms.

2.1. Digital image correlation

A grayscale camera measures the light intensity field $I(x, y)$ [55]. A grayscale image is represented by a 2D array of pixels, where the value of each pixel represents the amount of light; i.e. light intensity. Therefore, each image contains discrete values of the light intensity field that can be utilized to track the motion. The goal of DIC is to align a template image $T(x, y)$ with an input image $I(x, y)$ [6]:

$$\min_{\delta x, \delta y} \sum_{p} \left[T(x, y) - I(x + \delta x, y + \delta y)\right]^2, \tag{1}$$

where p is the pixels in a subset of pixels in an image, typically $q \times q$ pixels and δx and δy represent the incremental displacements. Each subset of pixels is referred to as a feature. DIC uses multiple pixels as opposed to a single one to avoid potential ambiguity with respect to the global motion direction, which is related to the aperture problem illustrated in Fig. 1 [59]. The resolution potential of the extracted motion is expected to increase linearly with respect to size q [55]. Residual errors may occur when solving the optimal incremental displacement in Eq. (1). To minimize the residuals, a new image is created by translating one of the images by δx and δy, after which Eq. (1) is reevaluated. The optimal global displacements (Δx and Δy) are found by updating after each increment:

$$\begin{aligned} &\Delta x \leftarrow \Delta x + \delta x, \text{ and} \\ &\Delta y \leftarrow \Delta y + \delta y. \end{aligned} \tag{2}$$

DIC retrieves incremental displacements and updates the global displacements until the displacement converges, typically by checking if the norm of the incremental displacements is below a threshold ϵ, *i.e.* $\|\delta \mathbf{x}\| \leq \epsilon$. As images are represented as 2D discrete grids located at integer coordinates, an interpolation function of one of the images needs to be generated to translate one of the images. A cubic interpolation function is used, which ensures the continuity and smoothness of the intensity field with high accuracy and convergence rate [56,60]. While Eq. (1) includes only translations, the method is often extended to include more involved transformations, for example, affine warp [61]. Previous work has shown that for small displacement (sub-pixel), as is often the case in structural vibration, extracting only translations can significantly decrease the computation time and noise in results [32]. DIC can be implemented in various ways; for a comparison of different methods and a detailed derivation of the method, refer to, for example, Baker et al. [7]. In the implementation of this work, an interpolation function is set up only once for the template image rather than for each frame in the video. Firstly, this is advantageous as it enables precomputing the interpolation function [62]. Secondly, as the template image can be denoised, a higher-quality interpolation function can be created leading to better results [7]. Denoising the template image is achieved by averaging a set of frames in the time domain instead of using, for example, the first frame in the video [63]. In the case of small amplitude (sub-pixel) harmonic vibrations, T can be acquired by averaging all frames since harmonic displacement does not, mathematically, affect the average pixel intensity level [55]. For high amplitude vibrations

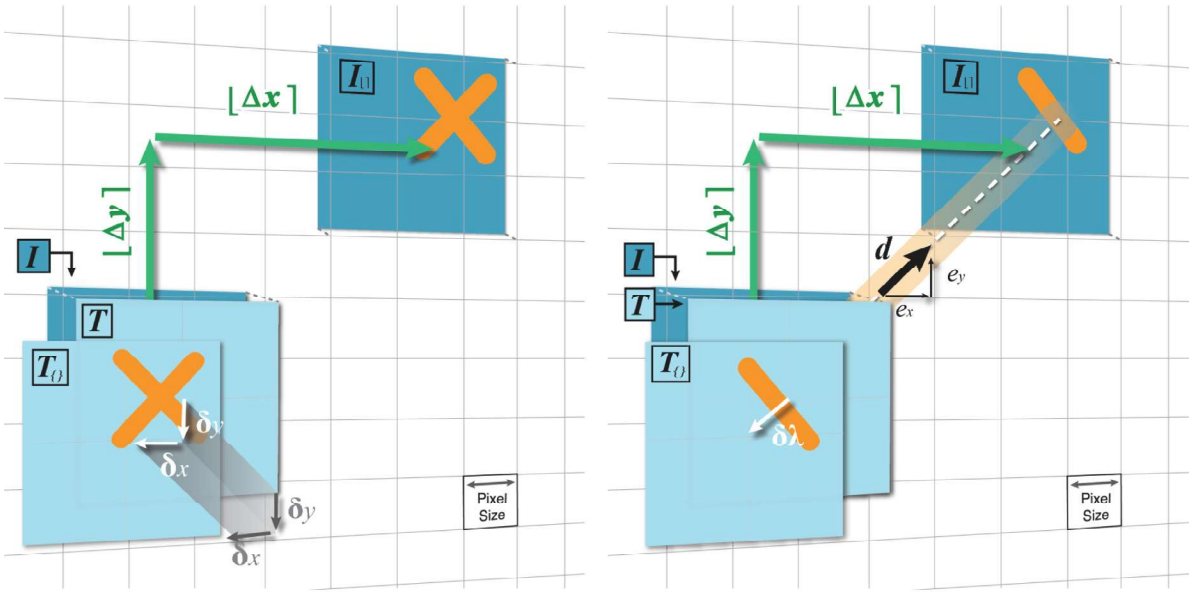

(a) Template image T is shifted with the incremental displacements δx and δy, and input image I is shifted with integer displacements $\lfloor \Delta x \rceil$ and $\lfloor \Delta y \rceil$, to align a feature that has a high gradient in two orthogonal directions (a cross).

(b) Template image T is shifted with incremental displacement $\delta\lambda$ in direction $\mathbf{d}$, and image I is shifted with integer displacements $\lfloor \Delta x \rceil$ and $\lfloor \Delta y \rceil$, to align a feature that has a high gradient in direction $\mathbf{d}$ (an edge).

Fig. 2. A schematic depiction of (a) conventional DIC, and (b) Directional DIC. Both set up with $q = 3$.

(multi-pixel), T can still be averaged but only on frames before applying an excitation [63]. The DIC implementation is modified to ensure that only the template image needs to be interpolated. The global displacements are split into the nearest pixel integer (the pixel shift, $\lfloor \Delta x \rceil$ and $\lfloor \Delta y \rceil$) and its corresponding residuals Δx and Δy:

$$\begin{aligned} \Delta x &= \lfloor \Delta x \rceil + \{\Delta x\}, \text{ and} \\ \Delta y &= \lfloor \Delta y \rceil + \{\Delta y\}. \end{aligned} \tag{3}$$

This specific split ensures that an image shifted with $\lfloor \Delta x \rceil$ and $\lfloor \Delta y \rceil$ is directly accessible from memory. The goal function, *i.e.* Eq. (1), is then modified into:

$$\min_{\delta x, \delta y} \sum_{p} \left[T_{\{\}}(x - \delta x, y - \delta y) - I_{\lfloor\rceil}(x, y) \right]^2 . \tag{4}$$

where $T_{\{\}}$ is the interpolated template image, and $I_{\lfloor\rceil}$ the pixel shifted input image, or:

$$T_{\{\}}(x, y) = T(x - \{\Delta x\}, y - \{\Delta y\}), \text{ and} \tag{5}$$

$$I_{\lfloor\rceil}(x, y) = I(x + \lfloor \Delta x \rceil, y + \lfloor \Delta y \rceil). \tag{6}$$

The residual displacements are updated according to:

$$\begin{aligned} \{\Delta x\} &\leftarrow \{\Delta x\} + \delta x, \text{ and} \\ \{\Delta y\} &\leftarrow \{\Delta y\} + \delta y. \end{aligned} \tag{7}$$

After convergence, the optimal global displacements are found via Eq. (3). The DIC implementation is depicted in Fig. 2(a).

The optimal incremental displacements in Eq. (4) are obtained by taking the first-order Taylor expansion of $T_{\{\}}$ with respect to x and y and setting the resulting equation to zero. The spatial derivatives of $T_{\{\}}$ are switched with those of $I_{\lfloor\rceil}$ following the Hager-Belhumeur implementation [62]. This is a justified replacement as $T_{\{\}} \approx I_{\lfloor\rceil}$, provided that the initial approximations of the global displacements are close to the truth. The replacement provides a computational advantage as $\frac{\partial I}{\partial \mathbf{x}}$ remains constant in each iteration and thus only needs to be computed once per frame. The incremental displacements are then retrieved as follows:

$$\begin{bmatrix} \delta x \\ \delta y \end{bmatrix} = H^{-1} \sum_{p} \begin{bmatrix} \frac{\partial I}{\partial x} \\ \frac{\partial I}{\partial y} \end{bmatrix} \left(I_{\lfloor\rceil} - T_{\{\}} \right), \tag{8}$$

Fig. 3. Automatic feature selection in a spiderweb-like cable network. (a) A template image T is established. (b) T is filtered, for example, with λ_0 to create the score image S. (c) Features are selected automatically from S with an algorithm, for example, in descending order of score, at local maxima, or with ANMS.

where H is the (Gauss–Newton approximation to the) Hessian matrix:

$$H = \sum_p \begin{bmatrix} \left(\frac{\partial I}{\partial x}\right)^2 & \frac{\partial I}{\partial x}\frac{\partial I}{\partial y} \\ \frac{\partial I}{\partial x}\frac{\partial I}{\partial y} & \left(\frac{\partial I}{\partial y}\right)^2 \end{bmatrix}. \tag{9}$$

2.2. Automatic feature selection

An automatic feature selection algorithm first quantifies all potential tracking locations in T based on its expected tracking performance to create a score image S, as shown in Fig. 3. Subsequently, an algorithm selects features from the score image, for example, with one of the algorithms discussed later in this section. Good features to track have high gradients in two orthogonal directions to overcome the aperture problem, as seen in Fig. 1. This observation can be formalized by inspecting Eq. (8). A smaller displacement can be measured for the same amount of difference between $I_{[]}$ and $T_{\{\}}$ if H is big, *i.e.* the sensitivity of Eq. (8) increases as H increases. Additionally, Eq. (8) will be stable if H is easily invertible, *i.e.* H is well-conditioned. The symmetric matrix H is well conditioned if $|\lambda_1| / |\lambda_0| \approx 1$, with λ_0 and λ_1 being the smaller and the larger eigenvalue of H, respectively. In practice, H will be well-conditioned if the smaller eigenvalue is large. This comes from the fact that the pixel intensity gradients will be bounded by the minimum and maximum pixel intensity value, such that the greater eigenvalue cannot be arbitrarily large [50]. This led Tomasi et al. to introduce the smallest eigenvalue to score the tracking performance [50].

$$\lambda_0 = \min(\text{eigvals}(H)) \tag{10}$$

The score image S is then created by applying Eq. (10) as a filter across the template image. The kernel size of the filter matches the subset size q used in DIC. Next, an algorithm selects locations based on S. This theoretical background provides three possible algorithms for automatic feature selection. In Algorithm 1, tracking locations are sorted based on scores in S, and features are picked in descending order of score [50,51]. This algorithm excludes features that overlap with windows of size w centered at previously selected features. The size of the subsets, q, does not have to match that of the windows, w, used for excluding feature locations. This allows for control over how spread-out features will be selected across the structure. In algorithm 2, local maxima in a window of size w are retrieved from S. The highest n local maxima are set as features [49,52]. Tuning w provides control over the spread out n features across a structure. Algorithm 3 applies the Adaptive Non-Maximal Suppression (ANMS) algorithm to select features that are evenly spread out across an image [53]. This can be useful in experimental modal analysis, for example, when structures are unevenly illuminated or patterned across the structure. ANMS starts with a list of local maxima in the score image retrieved with, for example, the local maxima algorithm with $w = 3$. Next, the radius for which the potential feature location is a local maximum is retrieved. The maxima are then ordered in descending order of radius, and the largest n radii are added as features. The algorithm robustness is improved by using a robustifying factor c to retrieve the radius R where the maximum is significantly higher than its neighbors.

Algorithm 1: Select by descending score excluding overlapping windows, based on [50,51]

Input: Score image S, window size w, number of features n
Output: f: a List of n feature locations

```
w = w // 2;
Sort the pixel locations in S in descending order of score;
initialize an empty list f;
for pixel location (x, y) in the ordered list do
    if any pixel locations (x − w − 1 : x + w, y − w − 1 : y + w) is in f then
        Continue to the next pixel location;
    end
    Add the pixel locations (x, y) to f;
    if The number of features in f equals n then
        Exit the loop;
    end
end
```

Algorithm 2: Select at local maxima, based on [49,52]

Input: Score image S, window size w, number of features n
Output: f: a list of n feature locations

Apply a maximum filter of size w to the score image S to obtain S^{f}, the filtered score image;
Identify local maxima in S by finding locations where $S^{\mathrm{f}}(x,y) = S(x,y)$;
Sort the local maxima in descending order based on their scores in S;
Select the first n locations from the sorted list as the feature locations f;

Algorithm 3: ANMS algorithm, based on [53]

Input: List of potential feature locations f^0, score image S, number of features n, robustifying factor c
Output: f: List of n feature locations

Sort the potential feature locations f^0 in descending order based on their scores in S;
Initialize an array R with ∞ for each f_i^0 in f^0;
for *each potential feature location* f_i^0 *in* f^0 **do**
  for *each potential feature location* f_j^0 *in* $f_{1:i-1}^0$ **do**
    if $c \cdot S(f_j^0) > S(f_i^0)$ **then**
      Compute the distance $r = \|f_i^0 - f_j^0\|_2$;
      if $r < R_i$ **then**
        $R_i = r$;
      end
    end
  end
end
Select the locations in f^0 corresponding to the largest n values in R as f;

3. Directional DIC with automatic feature selection

Section 3.1 details the mathematical development of the D-DIC method. The fundamental innovation in Section 3.2 is the introduction of parameter λ_{d} for facilitating accurate and efficient automatic feature selection. In Section 3.3, the effects of a discrepancy between the pre-defined motion direction and the real motion direction are discussed. Finally, the relationship between the subset size of a feature and the accuracy of the method is provided in Section 3.4.

3.1. Directional DIC

The D-DIC method assumes the motion to be in a single direction $\mathbf{d} = [e_x, e_y]^T$, with $|\mathbf{d}| = 1$. Let $\delta\lambda$ be the incremental displacements in $\mathbf{d}$. Thus, simple coordinate transformations can be achieved, such that $\delta x = \delta e_x \lambda$, and equivalent in y-direction. The DIC method is modified accordingly, and depicted in Fig. 2(b). The algorithm is modified accordingly by, first, applying the coordinate transformation to the goal function (4), such that:

$$\min_{\delta\lambda} \sum_p \left[T_{\{\}}(x - \delta e_x\lambda, y - \delta e_y\lambda) - I_{[]}(x,y)\right]^2. \tag{11}$$

The residual displacements $\{\Delta x\}$ and $\{\Delta y\}$ after applying the coordinate transformation are updated according to (see Eq. (7) for comparison):

$$\begin{aligned} &\{\Delta x\} \leftarrow \{\Delta x\} + \delta e_x \lambda, \text{ and} \\ &\{\Delta y\} \leftarrow \{\Delta y\} + \delta e_y \lambda. \end{aligned} \tag{12}$$

To solve the incremental displacement $\delta\lambda$, the nonlinear goal function, in Eq. (11), is linearized by performing a first order Taylor expansion on $T_{\{\}}$ with respect to λ:

$$\min_{\delta\lambda} \sum_p \left[T_{\{\}} + \frac{\partial T_{\{\}}}{\partial \lambda}\delta\lambda - I_{[]}\right]^2. \tag{13}$$

The spatial derivative with respect to λ is obtained efficiently from the spatial gradients with respect to x and y using the coordinate transformation (Eq. (14)). Similar to conventional DIC in Section 2.1, the implementation of D-DIC switches the spatial derivatives of $T_{\{\}}$ and $I_{[]}$, to improve computational efficiency, as follows:

$$\frac{\partial T_{\{\}}}{\partial \lambda} \approx \frac{\partial I_{[]}}{\partial \lambda} = e_x \frac{\partial I_{[]}}{\partial x} + e_y \frac{\partial I_{[]}}{\partial y}. \tag{14}$$

The derivative with respect to λ is retrieved, and the equation is set to zero. Accordingly, $\delta\lambda$ becomes:

$$\delta\lambda = \frac{1}{\sum_p \left(\frac{\partial I_{[]}}{\partial \lambda}\right)^2} \sum_p \frac{\partial I_{[]}}{\partial \lambda}(I_{[]} - T_{\{\}}). \tag{15}$$

In short, the D-DIC algorithm loops the following steps until convergence is reached, $|\delta\lambda| \leq \epsilon$:

- interpolate $T_{\{\}}$ with the residual displacements using Eq. (5);
- retrieve the incremental displacement $\delta\lambda$ via Eq. (15); and
- update the residual displacements via Eq. (12).

Finally, the global displacements are found after accounting for the integer pixel shift using Eq. (3).

3.2. Automatic feature selection for directional DIC

In conventional DIC, a feature requires a high pixel intensity gradient in two orthogonal directions to overcome the aperture problem and ensure high sensitivity, as established in Section 2.2. Since Directional DIC uses a predetermined motion direction, it experiences a reduced influence from the aperture problem. Consequently, the requirements for a feature will be different. The displacement in direction $\mathbf{d}$ is observable when the gradient is high. This can be formalized by inspecting Eq. (15). As the gradient in $\mathbf{d}$ increases, smaller displacement can be observed for the same amount of difference between $I_{[]}$ and $T_{\{\}}$, *i.e.* the sensitivity of D-DIC increases as $\frac{I_{[]}}{\partial\lambda}$ increases. This observation is captured in parameter λ_{d}, which sums the intensity gradient in $\mathbf{d}$ for a subset of pixels in a feature. Taking the absolute value ensures that the parameter highlights gradients in both positive and negative directions.

$$\lambda_{\mathrm{d}} = \sum_{p} \left| e_x \frac{\partial T}{\partial x} + e_y \frac{\partial T}{\partial y} \right| \tag{16}$$

As λ_{d} is less strict than λ_0 in general more features can be selected on the same structure, especially for non-ideal surface patterns. Parameter λ_{d} is a similar feature to the Sum of Square of Subset Intensity Gradients (SSSIG) proposed by Pan et al. [64]. In contrast to SSSIG, λ_{d} will only highlight features with intensity gradients in the appropriate direction. When all tracking locations are quantified with λ_{d}, features can be selected with, for example, one of the algorithms described in Section 2.2.

3.3. The assumption of single directional displacement

Directional DIC is facilitated by assuming a constant pre-determined displacement direction $\mathbf{d}$. In practical cases, one must consider that the actual displacement direction may not be constant, and there may be a discrepancy between the actual and assumed displacement directions. This raises the question of what the effect of error in the assumed displacement direction $\mathbf{d}$ is on the robustness and the accuracy of the D-DIC method. Consider a case where there is displacement perpendicular to $\mathbf{d}$, denoted as $\mathbf{d}^{\perp}$. When the tracked feature has no gradient in $\mathbf{d}^{\perp}$ (a perfect edge along $\mathbf{d}^{\perp}$), it will not affect the robustness, as the pixel intensity value will remain constant independent of the displacement in $\mathbf{d}^{\perp}$. However, if there is a gradient in $\mathbf{d}^{\perp}$, the correlation between $I_{[]}$ and $T_{\{\}}$ will decrease as the displacement in $\mathbf{d}^{\perp}$ increases, meaning that the expected robustness of D-DIC will decrease. In general, the expected robustness of D-DIC increases as the gradient in $\mathbf{d}^{\perp}$ within a feature decreases.

We can analyze the effects of displacement in $\mathbf{d}^{\perp}$ on the accuracy of D-DIC using trigonometry. Consider the sub-pixel displacement of an individual pixel in a feature, shown in Fig. 4; where α is the offset angle between the predefined motion direction $\mathbf{d}$ and the actual motion direction $\mathbf{d}^{*}$; and β is the angle between the gradient direction of the pixel of interest ($\nabla\mathbf{I}$) and $\mathbf{d}$. The direction of $\nabla\mathbf{I}$ is assumed to be constant for a sub-pixel displacement and is crucial as the optimal displacement of the pixel is perpendicular to it. The percentage error relative to the real displacement (AC) as a function of angles α and β is calculated between the real displacement in $\mathbf{d}$ (AD) and the measured displacement (AB), and it is represented by:

$$\text{error} = \frac{AD - AB}{AC} \cdot 100\% = \left(\cos(\alpha) - \frac{\cos(\alpha + \beta)}{(\cos\beta)} \right) \cdot 100\%. \tag{17}$$

Eq. (17) is plotted for several cases of β in Fig. 5. This analysis pertains to an individual pixel. Since the relationship in Eq. (17) is nonlinear, each pixel in a feature must be evaluated individually to determine the overall accuracy of the entire feature. Eq. (17) shows that the error is zero as long as β is exactly zero. However, in all other cases, the error increases as the offset error increases. Notably, the error can be especially significant when the pixel intensity gradient is poorly aligned with $\mathbf{d}$. Using such subsets is discouraged for cases where α is expected to be high during a test. When tracking features that do not look like straight edges, it is expected that the accuracy of the feature will be a mixture of low- and high-error pixels, some of which will cancel each other. In these cases, conventional DIC can also be used to identify displacement, as there will be a gradient in two orthogonal directions. Generally, the accuracy of a feature will increase when its pixel intensity gradient is aligned with $\mathbf{d}$.

3.4. Relationship robustness and subset size

While conventional DIC suffers from the aperture problem (the 2D motion is under-defined when using individual pixels), the D-DIC method has a pre-determined local motion direction. The aperture problem is, therefore, expected to play a less significant role, which should cause the proposed method to require smaller subsets to converge than conventional DIC. The theoretical resolution potential is related to the subset size ($q \times q$) and the bit depth of the camera n according to [55]:

$$\Delta x_{\min} = \frac{1}{(2^n - 1)q}. \tag{18}$$

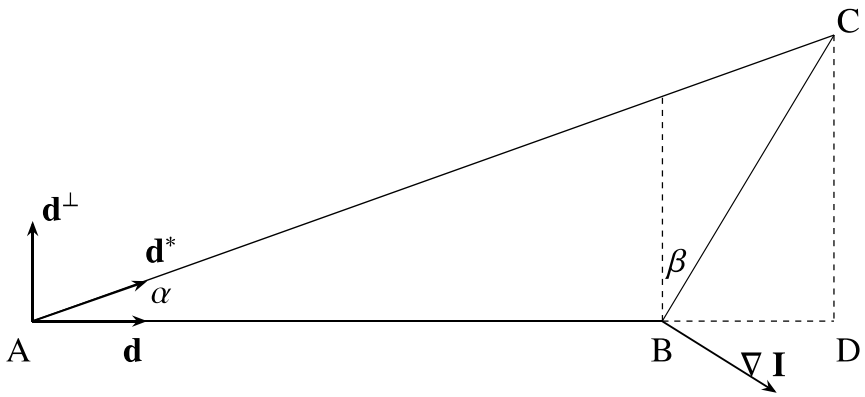

Fig. 4. Schematic of the displacement of an individual pixel in a feature during D-DIC, located at *A* moving to *C*. The vector **d** is the pre-determined motion direction. The real motion direction is $\mathbf{d}^*$. The offset angle between **d** and $\mathbf{d}^*$ is α. The gradient of the pixel of interest is $\nabla\mathbf{I}$. β is the angle between **d** and the direction of $\nabla\mathbf{I}$. *AC*: The real displacement of the pixel, *AB*: the measured displacement with D-DIC, and *AD*: the real displacement in **d**.

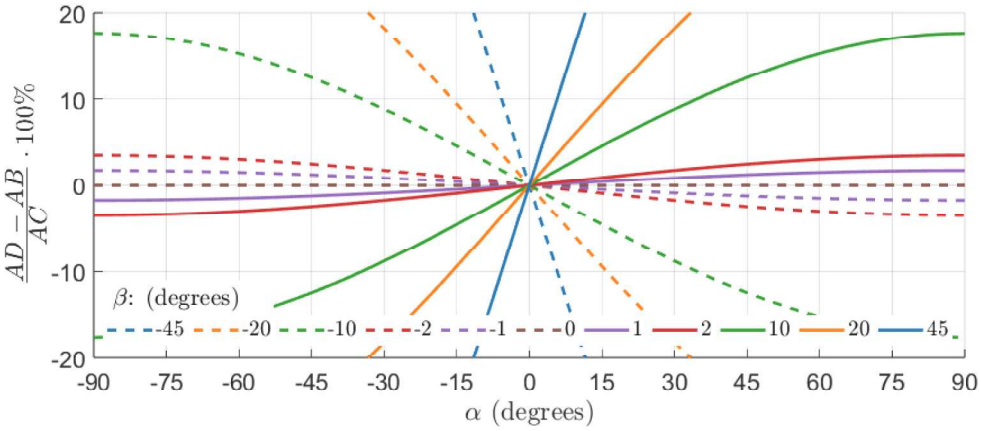

Fig. 5. The mathematical error of a single pixel in a feature as a function of the offset angle α between **d** and $\mathbf{d}^*$, for several cases of β, β is the angle between the pre-determined motion direction and the direction of the pixel intensity gradient of the pixel.

The implication is that the resolution can be increased by choosing a larger subset. When retrieving motion of non-overlapping subsets, smaller subsets can be more advantageous, as more features can be selected. The change in pixel intensity is proportional to the displacement, meaning that the camera noise maps to the displacement noise. By using more features, the displacement noise can be averaged out. Using the same pixel multiple times in an overlapping feature will not average out the noise, as the pixel will have the same inherent error anytime it is evaluated.

4. Experimental research

To validate the proposed D-DIC method, a modal analysis was conducted on a structure that does not have a high pixel-intensity gradient in two orthogonal directions across the whole structure. The methodology for gathering modal results – consisting of frequency response functions and vibration shapes – based on a sequence of images starts with choosing a feature size ($q \times q$) and feature locations. The feature size is typically selected through a parameter study. Feature locations can be selected either manually or automatically, employing suitable methods for conventional DIC (λ_0, see Section 2.2) or D-DIC (λ_d, see Section 3.2). To ensure that automatic feature selection exclusively adds features relevant to the structure of interest, pixels outside this structure can be automatically omitted by excluding pixels outside a user-defined region of interest. A template image is created from the image sequence. This can either be an individual image or an average of multiple images. Conventional and D-DIC is then employed to measure the displacements at the features using a user-defined tolerance ϵ. The motion direction d for D-DIC, can often be estimated visually. However, in cases where the motion direction is unclear, the displacement can be tracked at specific locations with DIC that meet the required gradient conditions. The direction d is then determined by calculating the slope of a linear fit through the resulting displacement path. Conventional and D-DIC is employed with the OpenSource PyIDI package [58]. In practice, it is found that not all features measure the displacement correctly. Therefore, three thresholds are proposed to classify a feature as (un)successful. If

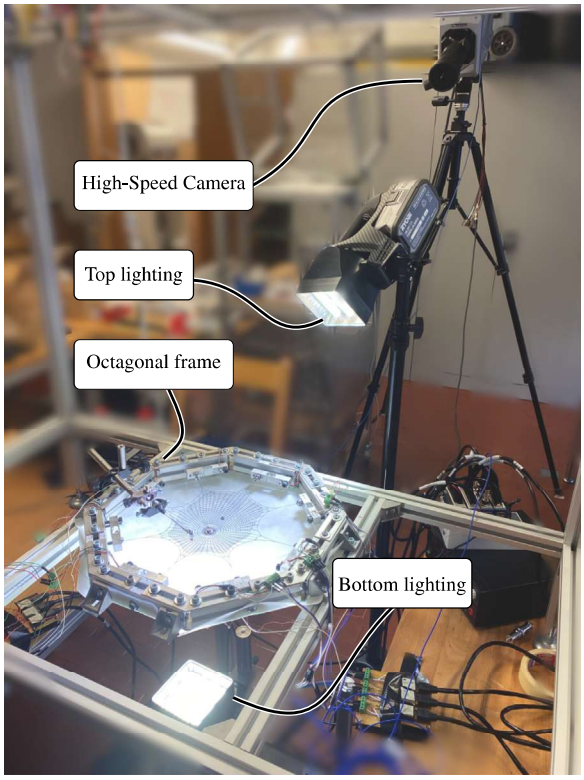

Fig. 6. Global test set-up. The High-Speed Camera is a Photron Fastcam SA-Z equipped with a Sigma 180 mm F2.8 Macro lens. Top and bottom lighting is achieved using two battery-powered 50 kLumen LED lights.

one of the following thresholds is met, the feature is classified as unsuccessful:

$$\begin{aligned} &(1): \text{The maximum retrieved displacement is greater than } a \text{ pixels.} \\ &(2): \text{The displacement between subsequent frames is bigger than } b \text{ pixels.} \\ &(3): \text{The displacement at the last frame is more than } c \text{ pixels.} \end{aligned} \tag{19}$$

The parameters a, b, and c are case-by-case dependent ones set by the user. The third threshold is proposed to identify features drifting along edge-like features in conventional DIC but will only catch features that drift by more than c pixels. As λ_0 should score low on edge-like features, a better practice is to exclude these features by setting fewer features. Finally, modal parameter estimation can be performed, and vibration modes are fitted.

4.1. Spiderweb-like structure

The experimental setup can be described as follows. A spiderweb-like structure was 3D printed using Thermoplastic polyurethane (TPU) material. The structure was printed from a single layer 0.2 mm thick and 0.4 mm wide. The distance between a connection point and its opposing one was 29 cm. The width and height of the spiral making up the web were 22 and 26 cm, respectively. The flexible low-mass structure was suspended within a frame, as shown in Fig. 6. Retrieving the dynamics of such structures with contact method sensors, such as accelerometers and strain gauges, is discouraged as they will alter the dynamics [65]. Alternative non-contact methods, such as the Laser Doppler Vibrometer, require repeated testing to retrieve the full field response [65]. Applying a speckle pattern to the thin structure was found to be inappropriate because the paint was intrusive to the material properties of the TPU, resulting in a single strand feeling less flexible and damping vibrations more quickly. The spiderweb-like structure was excited with a modal hammer in the out-of-plane direction, where out-of-plane unidirectional vibration was predominant. In the test, 8,000 frames were acquired at 8,000 frames/second with pixel values on a 12-bit grayscale and 1,024 × 512 pixels per frame. The structure was illuminated using two 50 kLumen LED lights, located at the top and bottom of the structure, with a light-diffusing panel located at the bottom, as shown in Fig. 6. This lighting approach ensured a high-intensity gradient between the structure (black) and the background (white).

A parameter study on the subset size revealed that for conventional DIC a subset size of 9 × 9 was optimal. The same subset sizes were used in conventional DIC as in D-DIC. Features are selected automatically inside of a region of interest, as depicted in Fig. 7. Features were placed at local maxima, using $w = 3$ (Algorithm 2). Features were added until the algorithm added features

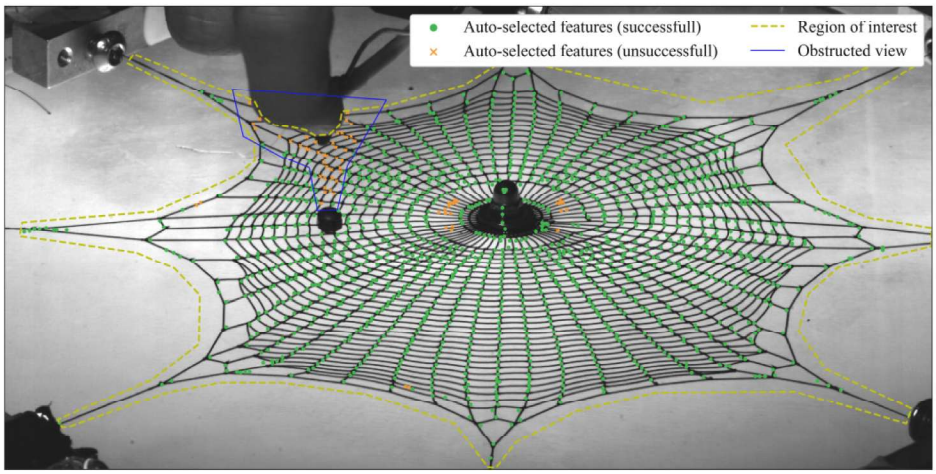

(a) Conventional DIC: 1,553 out of 1,600 automatically selected features tracked successfully. When excluding features with an obstructed view, 1,521 out of 1,545 features were tracked successfully (success rate of 0.984).

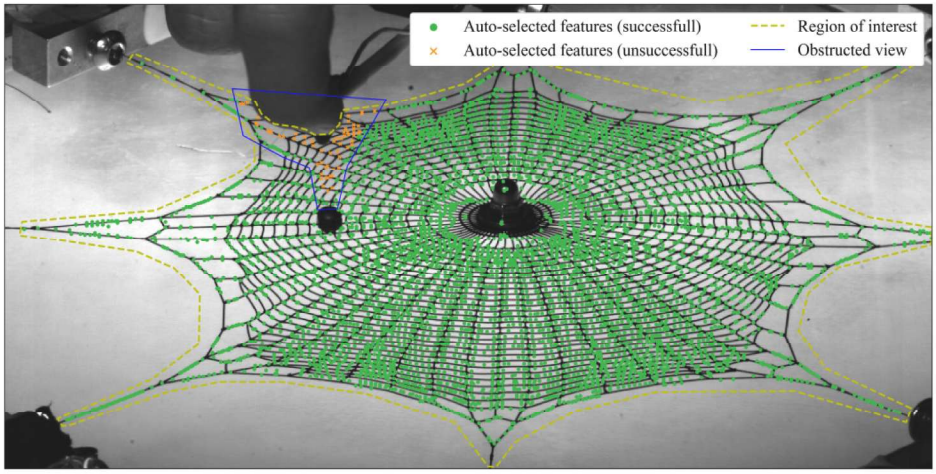

(b) Directional DIC: 5,340 out of 5,400 automatically selected features tracked successfully. When excluding features with an obstructed view, 5292 out of 5292 features were tracked successfully (success rate of 1.0).

Fig. 7. The automatically selected features for DIC and D-DIC with a subset size of 9 × 9. Only pixels inside the region of interest were considered as possible feature locations.

on edge-like features for conventional DIC, or in the background for D-DIC. For both methods, a denoised template image T was generated by averaging the first 150 frames prior to the impact hammer impacting the web. Conventional or Directional DIC is employed with a tolerance of $\epsilon = 1 \cdot 10^{-8}$. The displacement in the video was visually determined to be predominately vertical, so, D-DIC was evaluated with $\mathbf{d} = [0, 1]^T$. To classify features as (un)successful, the following parameters were used in the thresholds in Eq. (19): $a = 6$, $b = 1$, and $c = 2$. Next, modal parameter identification was performed using the Least Square Frequency Domain method [66]. Poles were extracted between 5 and 300 Hz with polynomials up to order 150. Finally, mode shapes were fitted at stable poles.

For conventional DIC, 1,600 features were added using the algorithm, and 1,553 out of 1,600 were classified as successful. The algorithm mainly selected features at parts of the structure where strands intersect, such that the feature had high gradients in two orthogonal directions. For D-DIC, the algorithm was able to add significantly more features; 5,340 out of 5,400 were classified as successful. Many of the features failed to track the motion because the impact hammer obstructed the field of view at one or more frames in the video. When only including the features outside of the obstructed view, 1,521 out of 1,545 features were tracked successfully for conventional DIC (success rate of 0.984). However, 5,292 out of 5,292 features were tracked successfully for D-DIC (success rate of 1.0). The noise floor of the mean frequency response functions was higher in conventional DIC than in D-DIC, as highlighted in Fig. 8. This enabled D-DIC to identify more stable poles and vibration shapes than conventional DIC. For clarity,

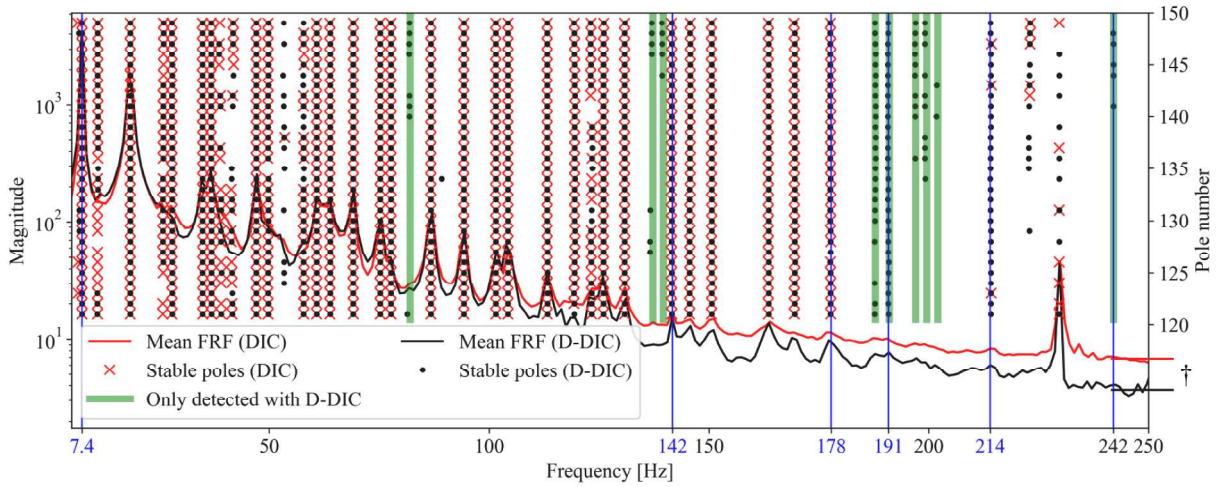

Fig. 8. Stability diagrams of the results with a subset size of 9 × 9 Poles are retrieved with the Least Squares Frequency Domain method, with only the stable poles depicted. Vertical blue annotations indicate the selection of modes depicted in Fig. 9. † The noise floor difference between DIC and D-DIC.

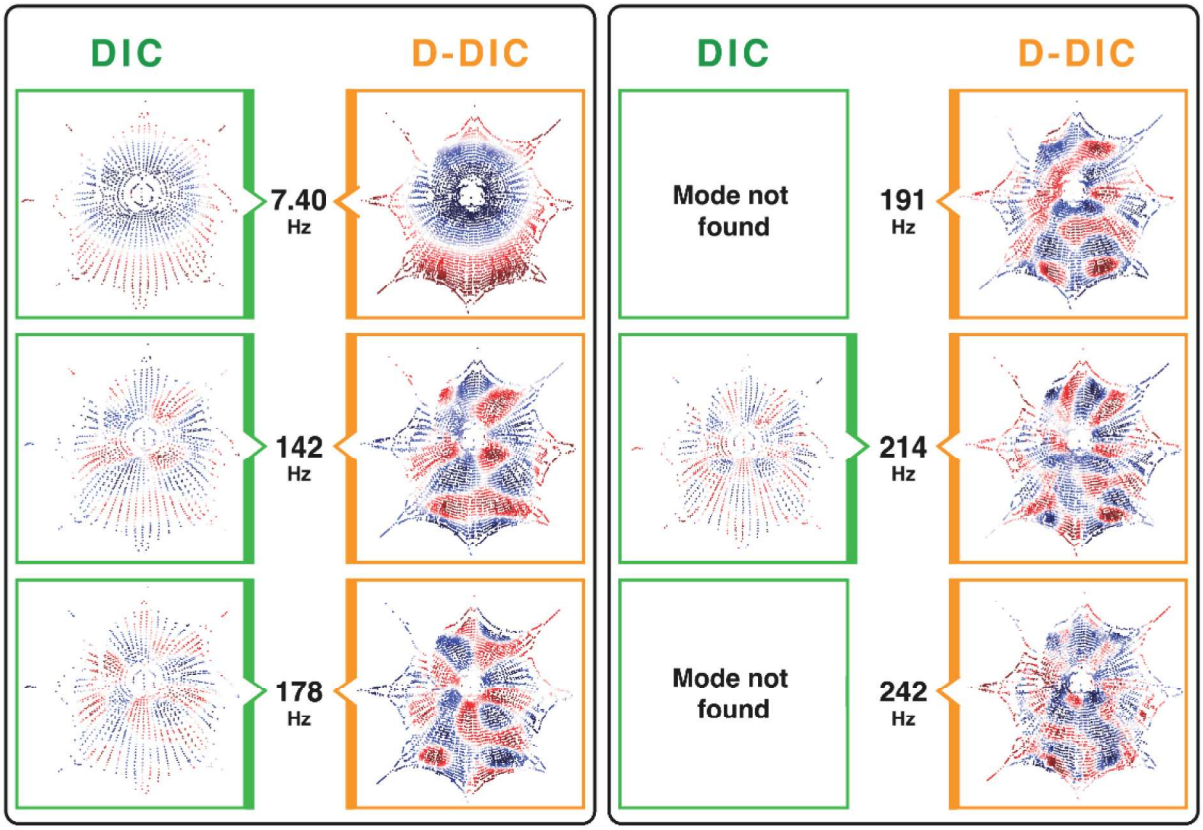

Fig. 9. Selection of mode shapes of the spiderweb-like structure comparing conventional DIC (DIC) with Directional DIC (D-DIC) method.

only the poles between polynomial order 120 and 150 are depicted in Fig. 8. The poles highlighted in green indicate those that were identified using D-DIC. The vibration shapes of the poles highlighted in blue vertical lines are shown in Fig. 9. As D-DIC allowed for setting significantly more appropriate features, the vibration shapes were more spatially dense. This made analyzing the characteristic shapes of the vibration shapes easier, especially those at high frequencies.

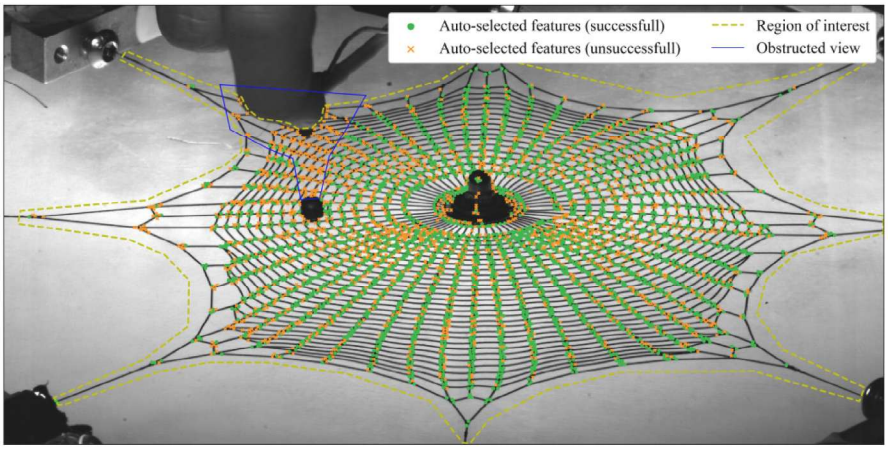

(a) Conventional DIC: 3,050 out of 5,000 features tracked successfully. When excluding features with an obstructed view, 3,040 out of 4,846 features were tracked successfully (success rate of 0.627).

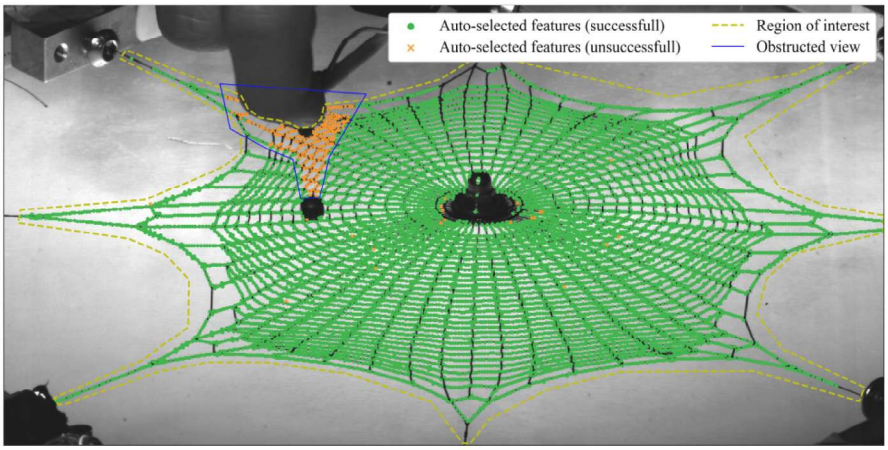

(b) Directional DIC: 10,076 out of 10,300 features tracked successfully. When excluding features with an obstructed view, 10,014 out of 10,035 features were tracked successfully (success rate of 0.998).

Fig. 10. The automatically selected features for DIC and D-DIC with a subset size of 3 × 3. Only pixels inside the region of interest were considered as possible feature locations.

4.2. Small subsets

In Section 2, it was noted that in conventional DIC, subsets of pixels are used to overcome the aperture problem. In this section, we show why the aperture problem is expected to play a less significant role since D-DIC uses a predetermined displacement direction. This was validated by retrieving the displacement of the web structure with a 3 × 3 subset size. Features were added in descending order of expected tracking performance, using $w = 3$ (Algorithm 1). The selected features shown in Fig. 10 are for the same parameters used in Section 4.1; $\epsilon = 1 \cdot 10^{-8}$, $\mathbf{d} = [0, 1]^T$, $a = 6$, $b = 1$, and $c = 2$. Modal parameter identification was performed using the Least Square Frequency Domain method between 5 and 300 Hz up to a polynomial order of 150. For conventional DIC, 5,000 features were added, of which 4,846 were outside the area with an obstructed view. When attempting to add more features, the algorithm predominantly added non-trackable edge-like features. Of the added features, 3,040 out of 4,846 characterized the displacement successfully (success rate of 0.627). For D-DIC, 10,300 features were successfully added, of which 10,035 were outside the area with an obstructed view. Beyond this point, the algorithm began incorporating features that were predominantly in the background. Of these features, 10,014 out of 10,035 characterized the displacement successfully (success rate of 0.998). The mean frequency response functions, in Fig. 11, show that the noise floor for D-DIC remained lower than for conventional DIC. More stable poles were identified, and vibration shapes were fitted using D-DIC. However, fewer stable poles were identified in comparison with larger subset sizes. This was as expected as the displacement resolution potential increases with the subset size q, as illustrated by Eq. (18).

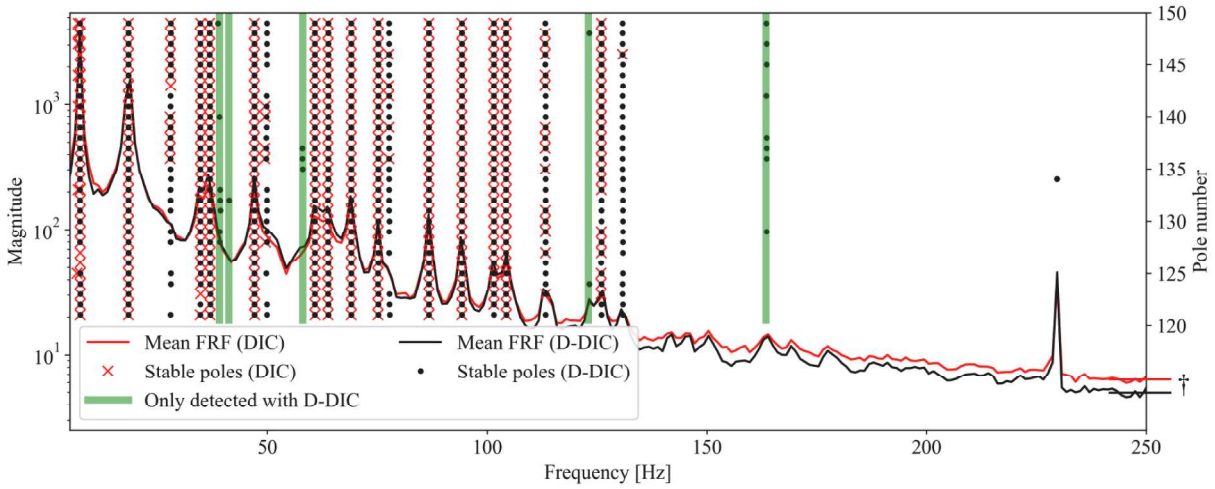

Fig. 11. Stability diagrams of the results with a subset size of 3 × 3. Poles are retrieved with the Least Squares Frequency Domain method, with only the stable poles depicted. † The noise floor difference between DIC and D-DIC.

5. Conclusion

The proposed Directional Digital Image Correlation (D-DIC) was a modification of the widely used DIC method by limiting the local displacement along a user-defined direction. The findings showed that D-DIC overcame several limitations in existing displacement estimators. The main limitation of using conventional DIC as a displacement estimator was that it had a strict requirement for features: a high pixel intensity gradient in two orthogonal directions. The requirement for a feature to be used with Directional DIC was less strict, as only a high gradient was required in the local displacement direction. This was validated by conducting a modal analysis for a spider web-like and highly flexible structure that did not have a well-defined pixel intensity gradient in two orthogonal directions across its full surface. More than three times as many features were tracked successfully with D-DIC than for conventional DIC for both large (9 × 9) and small (3 × 3) features. D-DIC was also better at tracking displacement when using smaller features than conventional DIC, which was indicative of the robustness of D-DIC against the aperture problem. For small features (3 × 3), conventional DIC only tracked the displacement with a success rate of 0.627 compared to 0.998 for Directional DIC. D-DIC enabled setting up a mean frequency response function that was less noisy. Finally, more stable poles and vibration shapes were retrieved with D-DIC than conventional DIC. Directional DIC was able to overcome SOF's small (sub-pixel) amplitude limitation by including a root-finding algorithm, as is conventional in DIC. The experimental analysis validated its accuracy at high displacement. The study demonstrated how to automatically select appropriate features for displacement estimation in a structure of interest. A parameter λ_d was proposed to be used for an automatic feature selector for uni-directional image-alignment techniques, such as Directional DIC. λ_d summed the pixel intensity gradient of a feature in the direction of the pre-defined displacement direction and takes the absolute value. Directional DIC enabled optical methods for cases where a speckle pattern could not be applied, but the motion was predominately uni-directional.

CRediT authorship contribution statement

Thijs Masmeijer: Writing – review & editing, Writing – original draft, Visualization, Validation, Software, Methodology, Investigation, Formal analysis, Data curation, Conceptualization. **Ed Habtour:** Writing – review & editing, Supervision, Resources, Project administration, Methodology, Investigation, Funding acquisition, Conceptualization. **Klemen Zaletelj:** Writing – review & editing, Software, Formal analysis, Data curation. **Janko Slavič:** Writing – review & editing, Supervision, Software, Resources, Project administration, Methodology, Funding acquisition, Data curation, Conceptualization.

Declaration of competing interest

The authors declare the following financial interests/personal relationships which may be considered as potential competing interests: Janko Slavic reports financial support was provided by Slovenian Research and Innovation Agency. Thijs Masmeijer reports financial support was provided by Boeing International Fellowship. If there are other authors, they declare that they have no known competing financial interests or personal relationships that could have appeared to influence the work reported in this paper.

Acknowledgments

The authors acknowledge partial financial support from the Slovenian Research Agency (research core funding No. P2-0263). They are also grateful for the Boeing International Fellowship, which supported Thijs Masmeijer as a summer visiting scholar to conduct the experiments at the University of Ljubljana in Slovenia.

Data availability

Data will be made available on request.

References

[1] E. Habtour, R. Sridharan, A. Dasgupta, M. Robeson, S. Vantadori, Phase influence of combined rotational and transverse vibrations on the structural response, Mech. Syst. Signal Process. 100 (2018) 371–383.

[2] R. Hou, Y. Xia, Review on the new development of vibration-based damage identification for civil engineering structures: 2010–2019, J. Sound Vib. 491 (2021) 115741.

[3] E. Habtour, D. Di Maio, T. Masmeijer, L. Cordova Gonzalez, T. Tinga, Highly sensitive nonlinear identification to track early fatigue signs in flexible structures, J. Nondestruct. Eval. Diagn. Progn. Eng. Syst. 5 (2) (2022) 021005.

[4] C. Warren, C. Niezrecki, P. Avitabile, P. Pingle, Comparison of FRF measurements and mode shapes determined using optically image based, laser, and accelerometer measurements, Mech. Syst. Signal Process. 25 (2011) 2191–2202, http://dx.doi.org/10.1016/J.YMSSP.2011.01.018.

[5] P.L. Reu, D.P. Rohe, L.D. Jacobs, Comparison of DIC and LDV for practical vibration and modal measurements, Mech. Syst. Signal Process. 86 (2017) 2–16, http://dx.doi.org/10.1016/J.YMSSP.2016.02.006.

[6] B.D. Lucas, T. Kanade, An iterative image registration technique with an application to stereo vision, in: IJCAI'81: 7th International Joint Conference on Artificial Intelligence, Vol. 2, Vancouver, Canada, 1981, pp. 674–679, URL https://hal.science/hal-03697340.

[7] S. Baker, I. Matthews, Lucas-Kanade 20 years on: A unifying framework, Int. J. Comput. Vis. 56 (2004) 221–255, http://dx.doi.org/10.1023/B:VISI.0000011205.11775.fd, URL http://link.springer.com/10.1023/B:VISI.0000011205.11775.fd.

[8] W.H. Peters, W.F. Ranson, Digital imaging techniques in experimental stress analysis, Opt. Eng., Bellingham 21 (1982) http://dx.doi.org/10.1117/12.7972925.

[9] M. Sutton, W. Wolters, W. Peters, W. Ranson, S. McNeill, Determination of displacements using an improved digital correlation method, Image Vis. Comput. 1 (1983) 133–139, http://dx.doi.org/10.1016/0262-8856(83)90064-1.

[10] T.C. Chu, W.F. Ranson, M.A. Sutton, Applications of digital-image-correlation techniques to experimental mechanics, Exp. Mech. 25 (1985) 232–244, http://dx.doi.org/10.1007/BF02325092.

[11] S.R. Atashipour, J. Baqersad, Noninvasive identification of directionally-dependent elastic properties of soft tissues using full-field optical data, J. Mech. Behav. Biomed. Mater. 151 (2024) 106266, http://dx.doi.org/10.1016/j.jmbbm.2023.106266.

[12] P. Olaszek, Investigation of the dynamic characteristic of bridge structures using a computer vision method, Measurement 25 (1999) 227–236, http://dx.doi.org/10.1016/S0263-2241(99)00006-8, URL https://linkinghub.elsevier.com/retrieve/pii/S0263224199000068.

[13] T.G. Ryall, C.S. Fraser, Determination of structural modes of vibration using digital photogrammetry, J. Aircr. 39 (2002) 114–119, http://dx.doi.org/10.2514/2.2903.

[14] C. Warren, C. Niezrecki, P. Avitabile, FRF measurements and mode shapes determined using image-based 3D point-tracking, in: Topics in Modal Analysis II, Vol. 6, Springer, 2011, pp. 243–252, http://dx.doi.org/10.1007/978-1-4419-9299-4_20, URL https://link.springer.com/10.1007/978-1-4419-9299-4_20.

[15] M.M. Wharton, Photogrammetry and mean intensity mapping as methods of low-cost structural health monitoring, Mech. Syst. Signal Process. 219 (2024) 111583, http://dx.doi.org/10.1016/j.ymssp.2024.111583.

[16] D.J. Fleet, A.D. Jepson, Computation of component image velocity from local phase information, Int. J. Comput. Vis. 5 (1990) 77–104, http://dx.doi.org/10.1007/BF00056772.

[17] M. Li, G. Liu, Z. Mao, Phased-based motion estimation through short-distance Hilbert transform, Mech. Syst. Signal Process. 211 (2024) 111219, http://dx.doi.org/10.1016/j.ymssp.2024.111219.

[18] Y. Yang, C. Dorn, T. Mancini, Z. Talken, G. Kenyon, C. Farrar, D. Mascareñas, Blind identification of full-field vibration modes from video measurements with phase-based video motion magnification, Mech. Syst. Signal Process. 85 (2017) 567–590, http://dx.doi.org/10.1016/j.ymssp.2016.08.041, URL https://linkinghub.elsevier.com/retrieve/pii/S0888327016303272.

[19] Y. Wang, W. Hu, J. Teng, Y. Xia, Full-field displacement measurement of long-span bridges using one camera and robust self-adaptive complex pyramid, Mech. Syst. Signal Process. 215 (2024) 111451, http://dx.doi.org/10.1016/J.YMSSP.2024.111451.

[20] T. Siebert, R. Wood, K. Splitthof, High speed image correlation for vibration analysis, J. Phys. Conf. Ser. 181 (2009) 012064, http://dx.doi.org/10.1088/1742-6596/181/1/012064, URL https://iopscience.iop.org/article/10.1088/1742-6596/181/1/012064.

[21] D. Gorjup, J. Slavič, M. Boltežar, Frequency domain triangulation for full-field 3D operating-deflection-shape identification, Mech. Syst. Signal Process. 133 (2019) 106287, http://dx.doi.org/10.1016/j.ymssp.2019.106287, URL https://linkinghub.elsevier.com/retrieve/pii/S0888327019305023.

[22] F. Renaud, S. Lo Feudo, J.-L. Dion, A. Goeller, 3D vibrations reconstruction with only one camera, Mech. Syst. Signal Process. 162 (2022) 108032, http://dx.doi.org/10.1016/j.ymssp.2021.108032.

[23] M.N. Helfrick, C. Niezrecki, P. Avitabile, T. Schmidt, 3D digital image correlation methods for full-field vibration measurement, Mech. Syst. Signal Process. 25 (2011) 917–927, http://dx.doi.org/10.1016/j.ymssp.2010.08.013.

[24] T.J. Beberniss, D.A. Ehrhardt, High-speed 3D digital image correlation vibration measurement: Recent advancements and noted limitations, Mech. Syst. Signal Process. 86 (2017) 35–48, http://dx.doi.org/10.1016/J.YMSSP.2016.04.014.

[25] R. Huňady, P. Pavelka, P. Lengvarský, Vibration and modal analysis of a rotating disc using high-speed 3D digital image correlation, Mech. Syst. Signal Process. 121 (2019) 201–214, http://dx.doi.org/10.1016/J.YMSSP.2018.11.024.

[26] P. Neri, A. Paoli, A.V. Razionale, C. Santus, Low-speed cameras system for 3D-DIC vibration measurements in the kHz range, Mech. Syst. Signal Process. 162 (2022) 108040, http://dx.doi.org/10.1016/j.ymssp.2021.108040.

[27] B.A. Furman, B.D. Hill, J.R. Rigby, J.M. Wagner, R.B. Berke, Sensor synchronized DIC: A robust approach to linear and nonlinear modal analysis using low frame rate cameras, J. Sound Vib. (2024) 118478, http://dx.doi.org/10.1016/J.JSV.2024.118478, URL https://linkinghub.elsevier.com/retrieve/pii/S0022460X24002414.

[28] C. Liu, A. Torralba, W.T. Freeman, F. Durand, E.H. Adelson, Motion magnification, ACM Trans. Graph. 24 (2005) 519–526, http://dx.doi.org/10.1145/1073204.1073223.

[29] K. Čufar, J. Slavič, M. Boltežar, Mode-shape magnification in high-speed camera measurements, Mech. Syst. Signal Process. 213 (2024) 111336, http://dx.doi.org/10.1016/j.ymssp.2024.111336, URL https://linkinghub.elsevier.com/retrieve/pii/S0888327024002346.

[30] K. Luo, X. Kong, J. Li, J. Hu, L. Deng, Motion magnification for video-based vibration measurement of civil structures: A review, Mech. Syst. Signal Process. 220 (2024) 111681, http://dx.doi.org/10.1016/j.ymssp.2024.111681.

[31] W. Wang, J.E. Mottershead, A. Ihle, T. Siebert, H.R. Schubach, Finite element model updating from full-field vibration measurement using digital image correlation, J. Sound Vib. 330 (2011) 1599–1620, http://dx.doi.org/10.1016/J.JSV.2010.10.036.

[32] K. Zaletelj, J. Slavič, M. Boltežar, Full-field DIC-based model updating for localized parameter identification, Mech. Syst. Signal Process. 164 (2022) 108287, http://dx.doi.org/10.1016/j.ymssp.2021.108287, URL https://linkinghub.elsevier.com/retrieve/pii/S088832702100652X.

[33] K. Zaletelj, D. Gorjup, J. Slavič, M. Boltežar, Multi-level curvature-based parametrization and model updating using a 3D full-field response, Mech. Syst. Signal Process. 187 (2023) 109927, http://dx.doi.org/10.1016/j.ymssp.2022.109927, URL https://linkinghub.elsevier.com/retrieve/pii/S0888327022009955.
[34] T.B. Abbott, F.-G. Yuan, Subsurface impact damage imaging for composite structures using 3D digital image correlation, Struct. Health Monit. 23 (2024) 568–587, http://dx.doi.org/10.1177/14759217231172297, URL http://journals.sagepub.com/doi/10.1177/14759217231172297.
[35] S. Yu, J. Zhang, C. Zhu, Z. Sun, S. Dong, Full-field deformation measurement and cracks detection in speckle scene using the deep learning-aided digital image correlation method, Mech. Syst. Signal Process. 209 (2024) 111131, http://dx.doi.org/10.1016/j.ymssp.2024.111131.
[36] T. Wu, L. Tang, F. Zhou, Y. Zhang, Z. Zhou, Damage detection based on accelerometers and computer vision measurements of moving load-induced structural responses, Mech. Syst. Signal Process. 211 (2024) 111246, http://dx.doi.org/10.1016/J.YMSSP.2024.111246.
[37] S. Zhang, P. Ni, J. Wen, Q. Han, X. Du, J. Fu, Intelligent identification of moving forces based on visual perception, Mech. Syst. Signal Process. 214 (2024) 111372, http://dx.doi.org/10.1016/j.ymssp.2024.111372.
[38] K. Zaletelj, J. Slavič, J. Šonc, M. Boltežar, Strain experimental modal analysis of an Euler–Bernoulli beam based on the thermoelastic principle, Mech. Syst. Signal Process. 201 (2023) 110655, http://dx.doi.org/10.1016/j.ymssp.2023.110655.
[39] T. Jiang, G.T. Frøseth, S. Wang, Ø.W. Petersen, A. Rønnquist, A 6-DOF camera motion correction method using IMU sensors for photogrammetry and optical measurements, Mech. Syst. Signal Process. 210 (2024) 111148, http://dx.doi.org/10.1016/j.ymssp.2024.111148.
[40] C. Niezrecki, P. Avitabile, C. Warren, P. Pingle, M. Helfrick, E.P. Tomasini, A review of digital image correlation applied to structural dynamics, in: Proceedings of the American Control Conference, 2010, pp. 219–232, http://dx.doi.org/10.1063/1.3455461, URL https://pubs.aip.org/aip/acp/article/1253/1/219-232/773027.
[41] J. Baqersad, P. Poozesh, C. Niezrecki, P. Avitabile, Photogrammetry and optical methods in structural dynamics – A review, Mech. Syst. Signal Process. 86 (2017) 17–34, http://dx.doi.org/10.1016/J.YMSSP.2016.02.011.
[42] B.K. Horn, B.G. Schunck, Determining optical flow, Artificial Intelligence 17 (1981) 185–203, http://dx.doi.org/10.1016/0004-3702(81)90024-2.
[43] E.C. Hildreth, S. Ullman, The Measurement of Visual Motion (Ph.D. thesis), Massachusetts Institute of Technology, 1982.
[44] P. Anandan, A computational framework and an algorithm for the measurement of visual motion, Int. J. Comput. Vis. 2 (1989) 283–310, http://dx.doi.org/10.1007/BF00158167, URL http://link.springer.com/10.1007/BF00158167.
[45] D. Lecompte, A. Smits, S. Bossuyt, H. Sol, J. Vantomme, D.V. Hemelrijck, A. Habraken, Quality assessment of speckle patterns for digital image correlation, Opt. Lasers Eng. 44 (2006) 1132–1145, http://dx.doi.org/10.1016/j.optlaseng.2005.10.004.
[46] T. Jiang, G.T. Frøseth, A. Rønnquist, E. Fagerholt, A robust line-tracking photogrammetry method for uplift measurements of railway catenary systems in noisy backgrounds, Mech. Syst. Signal Process. 144 (2020) 106888, http://dx.doi.org/10.1016/j.ymssp.2020.106888.
[47] B.W. McCormick, Aerodynamics, Aeronautics, and Flight Mechanics, second ed., John Wiley & Sons, Nashville, TN, 1994, pp. 153–156.
[48] L. Meirovitch, Fundamentals of Vibrations, Waveland press inc., Long Grove, 2010, pp. 616–617.
[49] H.P. Moravec, Rover visual obstacle avoidance, in: International Joint Conference on Artificial Intelligence, 1981, URL https://api.semanticscholar.org/CorpusID:18232715.
[50] C. Tomasi, T. Kanade, Shape and motion from image streams: a factorization method, Proc. Natl. Acad. Sci. 90 (1991) 9795–9802, http://dx.doi.org/10.1073/pnas.90.21.9795, URL https://pnas.org/doi/full/10.1073/pnas.90.21.9795.
[51] J. Shi, Tomasi, Good features to track, in: Proceedings of IEEE Conference on Computer Vision and Pattern Recognition, CVPR-94, IEEE Comput. Soc. Press, 1994, pp. 593–600, http://dx.doi.org/10.1109/CVPR.1994.323794.
[52] C. Harris, M. Stephens, A combined corner and edge detector, in: Procedings of the Alvey Vision Conference 1988, Alvey Vision Club, 1988, pp. 23.1–23.6, http://dx.doi.org/10.5244/C.2.23, URL http://www.bmva.org/bmvc/1988/avc-88-023.html.
[53] M. Brown, R. Szeliski, S. Winder, Multi-image matching using multi-scale oriented patches, in: 2005 IEEE Computer Society Conference on Computer Vision and Pattern Recognition, Vol. 1, CVPR'05, IEEE, 2005, pp. 510–517, http://dx.doi.org/10.1109/CVPR.2005.235, URL http://ieeexplore.ieee.org/document/1467310/.
[54] B. Triggs, Detecting keypoints with stable position, orientation, and scale under illumination changes, 2004, pp. 100–113, http://dx.doi.org/10.1007/978-3-540-24673-2_9, URL http://link.springer.com/10.1007/978-3-540-24673-2_9.
[55] J. Javh, J. Slavič, M. Boltežar, The subpixel resolution of optical-flow-based modal analysis, Mech. Syst. Signal Process. 88 (2017) 89–99, http://dx.doi.org/10.1016/j.ymssp.2016.11.009.
[56] B. Pan, H.M. Xie, B.Q. Xu, F.L. Dai, Performance of sub-pixel registration algorithms in digital image correlation, Meas. Sci. Technol. 17 (2006) 1615–1621, http://dx.doi.org/10.1088/0957-0233/17/6/045.
[57] S. Baker, I. Matthews, Equivalence and efficiency of image alignment algorithms, in: Proceedings of the 2001 IEEE Computer Society Conference on Computer Vision and Pattern Recognition, Vol. 1, CVPR 2001, IEEE Comput. Soc, 2001, pp. I–1090–I–1097, http://dx.doi.org/10.1109/CVPR.2001.990652, URL http://ieeexplore.ieee.org/document/990652/.
[58] K. Zaletelj, D. Gorjup, J. Slavič, Ladisk/pyidi: release of the version v0.23 (v0.23), Zenodo, 2020, http://dx.doi.org/10.5281/zenodo.4017153.
[59] D. Marr, S. Ullman, Directional selectivity and its use in early visual processing, Proc. R. Soc. Lond. [Biol.] 211 (1981) 151–180, http://dx.doi.org/10.1098/rspb.1981.0001, URL https://royalsocietypublishing.org/doi/10.1098/rspb.1981.0001.
[60] H.W. Schreier, Systematic errors in digital image correlation caused by intensity interpolation, Opt. Eng., Bellingham 39 (2000) 2915, http://dx.doi.org/10.1117/1.1314593.
[61] J.R. Bergen, P. Anandan, K.J. Hanna, R. Hingorani, Hierarchical model-based motion estimation, in: G. Sandini (Ed.), Computer Vision — ECCV'92, Springer Berlin Heidelberg, Berlin, Heidelberg, 1992, pp. 237–252.
[62] G. Hager, P. Belhumeur, Efficient region tracking with parametric models of geometry and illumination, IEEE Trans. Pattern Anal. Mach. Intell. 20 (1998) 1025–1039, http://dx.doi.org/10.1109/34.722606, URL http://ieeexplore.ieee.org/document/722606/.
[63] F. Hild, S. Roux, Digital image correlation, in: Optical methods for solid mechanics. A full-field approach, Vol. 367, Wiley-VCH Weinheim (Germany), 2012, p. 76.
[64] B. Pan, H. Xie, Z. Wang, K. Qian, Z. Wang, Study on subset size selection in digital image correlation for speckle patterns, Opt. Express 16 (2008) 7037, http://dx.doi.org/10.1364/OE.16.007037.
[65] K.G. McConnell, P.S. Varoto, Vibration Testing, second ed., John Wiley & Sons, Nashville, TN, 2007, p. 168.
[66] P. Verboven, Frequency Domain System Identification for Modal Analysis (Ph.D. thesis), Vrije Universiteit Brussel, 2002.